

 Open access • Journal Article • DOI:10.1063/1.4772192

Large-eddy simulation of highly underexpanded transient gas jets — [Source link](#)

Ville Vuorinen, J. Yu, Santosh Tirunagari, Ossi Kaario ...+3 more authors

Published on: 08 Jan 2013 - Physics of Fluids (American Institute of Physics)

Topics: Shock diamond, Overall pressure ratio, Jet (fluid), Mach number and Shock (fluid dynamics)

Related papers:

- [A study of free jet impingement. Part 1. Mean properties of free and impinging jets](#)
- [Study of the highly underexpanded sonic jet.](#)
- [Free underexpanded jets in a quiescent medium: A review](#)
- [Large eddy simulation of highly turbulent under-expanded hydrogen and methane jets for gaseous-fuelled internal combustion engines](#)
- [Large-eddy simulation on the effect of injection pressure and density on fuel jet mixing in gas engines](#)

Share this paper:    

View more about this paper here: <https://typeset.io/papers/large-eddy-simulation-of-highly-underexpanded-transient-gas-3eunrbvbm>

Large-eddy simulation of highly underexpanded transient gas jets

V. Vuorinen,¹ J. Yu,¹ S. Tirunagari,¹ O. Kaario,¹ M. Larmi,¹ C. Duwig,²
 and B. J. Boersma³

¹*Department of Energy Technology, Aalto University School of Engineering, Finland*

²*Department of Energy Sciences, Lund University, Sweden*

³*Department of Energy Technology, Delft University of Technology, The Netherlands*

(Received 21 June 2012; accepted 9 November 2012; published online 8 January 2013)

Large-eddy simulations (LES) based on scale-selective implicit filtering are carried out in order to study the effect of nozzle pressure ratios on the characteristics of highly underexpanded jets. Pressure ratios ranging from 4.5 to 8.5 with Reynolds numbers of the order 75 000–140 000 are considered. The studied configuration agrees well with the classical picture of the structure of highly underexpanded jets. Similarities and differences between simulation and experiments are discussed by comparing the concentration field structures from LES and planar laser induced fluorescence data. The transient stages, leading eventually to the highly underexpanded state, are visualized and investigated in terms of a phase diagram revealing the shock speeds and duration of the transient stages. For the studied nozzle pressure ratio range, the Mach disk dimensions are found to be in good agreement with literature data and experimental observations. It is observed how the nozzle pressure ratio influences the Mach disk width, and thereby the slip line separation, which leads to co-annular jets with inner and outer shear layers at higher pressure ratios. The improved mixing with increasing pressure ratio is demonstrated by the probability density functions of the concentration. The coherent structures downstream of the Mach disk are identified using proper orthogonal decomposition (POD). The structures indicate a helical mode originating from the shear layers of the jet. Despite the relatively low energy content of the dominant POD modes, the frequencies of the POD time coefficients explain the dominant frequencies in the pressure fluctuation spectra. © 2013 American Institute of Physics. [<http://dx.doi.org/10.1063/1.4772192>]

I. INTRODUCTION

Compressible jets are encountered in a vast number of applications of which perhaps the best known lie within aerospace and aeronautics fields involving propulsion and aircraft design.^{1–7} Such high speed jets can also be observed in geophysical applications, for example, volcano eruptions release large amounts of gas in the atmosphere featuring weak shocks, compression waves and Mach-disks.⁸ Other examples are jet formation during accidental release of pressurized hydrogen through a small hole or a crack.⁹ Jets are present also in direct injection (DI) natural gas (NG) powered internal combustion engines where compressed natural gas is injected into the cylinder.^{10–12} Although the physics in all these examples is similar, the shape of the nozzles varies significantly from smoothly contoured, well designed nozzles for optimizing thrust in rocket engines to elongated and sharp holes in volcano and reservoir cracks. For example, the jet engine is designed to allow flexibility of flight operation, leading potentially to “double diamond” shock patterns.⁴ The fuel injection nozzles and jet engine exhaust lie somewhere in between the two extreme cases.^{13,14} Also the nozzle operating conditions, nozzle pressure ratio (NPR), depend on the application.

The literature implies that the driving motivation for studying jets varies from application to application. The background interest for this study lies in DI gas engines where the purpose is to design the injection conditions properly in order allow rapid mixing within some milliseconds prior

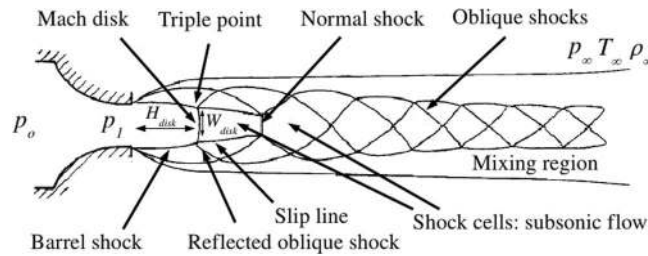


FIG. 1. The classical picture on the structure of a highly underexpanded jet. The picture is based on the visualization presented by Donaldson and Sneedeker.¹

to ignition. In DI gas engines, flow expansion, turbulent mixing downstream of the nozzle exit, and jet penetration are vital for the combustion process and emissions.^{10–14} Thereby, there is a need to better understand and to reliably predict supersonic jet formation from the viewpoint of (1) shock structures in the jet core, (2) turbulent mixing, and (3) coherent structures. In the present paper supersonic jets are studied using large-eddy simulations (LES). One of the general objectives of the paper are to enrich the present day views on transient, high Reynolds/Mach number jets encountered in DI gas engines.

The classical picture on the structure of a highly underexpanded jet is shown in Fig. 1 showing the Mach disk, the barrel shock, and the slip lines. At higher NPR , when $NPR > 10$, the empirical formula $H/D = C\sqrt{p_o/p_\infty}$ can be used to predict the Mach disk height.^{10,11} As H/D increases, also the distance between the slip lines increases. When $NPR \approx 4$ the Mach disk is very narrow and the slip lines are very close to one another.^{4–7} In the present paper we investigate the regime $4.5 \leq NPR \leq 8.5$ in order to gain further understanding into the effect of Mach disk width to the physics of highly underexpanded jets.

Donaldson and Sneedeker¹ have reviewed the previous experimental observations on the behavior of compressible jets issuing from convergent nozzles. The jets can be characterized by defining three reference pressures: (1) far upstream “reservoir” pressure p_o , (2) pressure at the nozzle exit p_1 , and (3) far downstream pressure p_∞ at ambient conditions where a free jet develops. The analysis¹ indicates three major jet flow regimes: (1) subsonic jet: $p_1/p_\infty = 1$, $1 < p_o/p_\infty < 1.893$, (2) moderately underexpanded jet: $1.1 < p_1/p_\infty \leq 2$, $2.08 < p_o/p_\infty < 3.8$, and (3) highly underexpanded jet: $2 < p_1/p_\infty$, $3.84 < p_o/p_\infty$. In moderately underexpanded conditions the jet exhibits the familiar oblique shock pattern (“shock diamonds”). In highly underexpanded conditions a normal shock, i.e., the Mach disk, forms. In particular, as p_o/p_∞ further increases the Mach disk increases in size.^{1,4,10–14} The presence of the Mach disk has also been reported for conditions which are relevant for combustion engines by White and Milton.¹²

The numerical framework for LES of subsonic and incompressible turbulent jets is well established^{15–22} and the recent studies have focused on supersonic conditions.^{23–30} A review on the classical and the state-of-the-art numerical methods for high-speed flows can be found in the review article by Pirozzoli.³¹ The challenges in LES of supersonic flows concern the simultaneous treatment of shocks and turbulence. One aims at capturing the discontinuity with simultaneously using accurate, centered schemes for the turbulent flow.³¹ LES subgrid scale (SGS) models for compressible flow with various levels of complexity have been discussed in the literature.¹⁷ A rather common model for turbulent dissipation is to apply a low-pass filter to the conservative variables as done by Bogey and Bailly.²¹ This approach has become rather popular in supersonic flows and it has been successfully applied by various authors.^{23–26,28–31} Typically the filter is chosen to be at least of the same order as the underlying numerical method in order to not decrease the order of the discretization. Even in direct numerical simulation (DNS), low-pass filtering is often employed for removal of dispersive and aliasing errors.³²

A common observation is that higher than second order filters are not sufficient for removing the Gibbs ringing near the shock discontinuities.³¹ Bogey *et al.*²³ proposed a method based on localized second order spatial filtering of the conservative variables at shock positions. They modeled turbulent dissipation with explicit high order filters.²¹ Cacqueray *et al.*²⁴ used a similar approach

for simulating the turbulent dynamics and shock cell structure of over-expanded jets. A few years ago, hyperviscosity for LES of shock-turbulence interactions was introduced by Cook and Cabot (CC).²⁸ The CC-model is based on augmenting the viscous stress tensor $\sigma_{ij} = \mu(\frac{\partial u_i}{\partial x_j} + \frac{\partial u_j}{\partial x_i}) + (\mu_b - \frac{2}{3}\mu)\frac{\partial u_i}{\partial x_j}\delta_{ij}$, with a modeled bulk viscosity μ_b . The approach²⁸ is appealing since it affects the flow only via the dilational part of the viscous stress. Thereby, the CC-model activates at shock fronts and deactivates in turbulent parts of the flow. A vast number of modifications to this model in the context of finite difference solvers have been proposed by, e.g., Kawai *et al.*²⁵ and Bhagatwala *et al.*,²⁹ Kawai and Lele²⁶ used the CC-model and explicit filtering for LES of a jet in supersonic cross-flow finding good agreement with experiments. They also demonstrated the presence of the Mach disk alongside with the strong presence of turbulence and acoustic fields. Mani *et al.*³⁰ showed how flow over a cylinder can be captured with a similar simulation method.

The previous examples^{23–26,28–31} are based on a high order finite difference framework. However, in more complex geometries finite volume methods (FVM) would be preferred. As mentioned by Pirozzoli,³¹ further studies on supersonic flows with unstructured FVM-codes are required. Recently, FVM was used in LES of a blunt body opposing a supersonic jet by Chen *et al.*³³ The dissipative elements in their simulations were: (1) central/upwind scheme for shock capturing and (2) explicit closure model for turbulence. LES of an impinging supersonic jet was carried out by Dauphain *et al.*⁵ using a third order accurate FVM code. The dissipative elements in their study were: (1) the CC-hyperviscosity for shock capturing, (2) explicit Smagorinsky model for turbulence closure, (3) upwind biased discretization of the convective terms, and (4) usage of tetrahedral mesh for the simulations. The observations^{5,33} motivate further developments and application of FVM for compressible jet flows.

In the present work large-eddy simulation (LES) of supersonic gas jets is carried out. The objectives are to (1) develop a gas jet injection model for LES of fuel jets, (2) use FVM for high speed flows³¹ and use the scale-selective discretization approach by Vuorinen *et al.*³⁴ for accounting for the turbulent dissipation, (3) better understand the physical consequences of the effect of jet injection pressure on shock formation, and (4) use proper orthogonal decomposition (POD) to characterize the dominant modes of the jets. As a numerical tool, we have implemented a density based 4th-order Runge-Kutta finite volume (FV) solver using the OpenFOAM[®] library.¹⁶ The FV-method on an unstructured grid framework is chosen since the method should be eventually applied in complex geometries. The results are qualitatively compared with planar laser induced fluorescence (PLIF) experiments.^{13,14} The organization of the paper is as follows: in Sec. II the numerical method is explained, and in Sec. III LES results from jet development and mixing are presented. Finally, in Sec. IV conclusions of the work are discussed.

II. NUMERICAL PROCEDURE

A. Governing equations

The dynamics of compressible flows are governed by the full Navier-Stokes equations $NS = NS(\rho, u_i, \dots) = 0$ describing the conservation of mass, momentum, and energy¹⁷

$$\frac{\partial \rho}{\partial t} + \frac{\partial \rho u_j}{\partial x_j} = 0, \quad (1)$$

$$\frac{\partial \rho u_i}{\partial t} + \frac{\partial (\rho u_i u_j)}{\partial x_j} = \frac{\partial}{\partial x_j} (-p \delta_{ij} + \sigma_{ij}), \quad (2)$$

$$\frac{\partial \rho e}{\partial t} + \frac{\partial ((\rho e + p) u_j)}{\partial x_j} = \frac{\partial}{\partial x_j} (\sigma_{ij} u_i) + \frac{\partial}{\partial x_j} \left(\lambda \frac{\partial T}{\partial x_j} \right), \quad (3)$$

where the quantities ρ , u_i , p , and T are respectively the density, velocity, pressure, and temperature of the gas. The pressure is explicitly coupled to the density and the temperature via the equation of

state

$$p = \rho RT. \quad (4)$$

Furthermore, the internal energy of the flow is defined as the sum of thermodynamic and kinetic energy

$$e = c_v T + 1/2 u_i u_i. \quad (5)$$

In Eq. (2) the viscous stress tensor is defined as follows:

$$\sigma_{ij} = \mu \left(\frac{\partial u_i}{\partial x_j} + \frac{\partial u_j}{\partial x_i} \right) + \left(\mu_b - \frac{2}{3} \mu \right) \frac{\partial u_i}{\partial x_j} \delta_{ij}, \quad (6)$$

where μ_b is the bulk viscosity of the gas and μ is the dynamic viscosity computed by Sutherland's law

$$\mu(T) = \mu_s \frac{T_s + C_s}{T + C_s} (T/T_s)^{1.5}. \quad (7)$$

In Eq. (7) $\mu_s = 1.781 \times 10^{-5}$ kg/ms, $T_s = 300.55$ K, and $C_s = 111.0$ K corresponding to the properties of nitrogen.

An additional equation for a passive scalar $c = c(x, y, z, t)$ is solved in order to study mixing:

$$\frac{\partial \rho c}{\partial t} + \frac{\partial \rho c u_j}{\partial x_j} = \frac{\partial}{\partial x_j} \rho D_c \frac{\partial c}{\partial x_j}, \quad (8)$$

where D_c is the species diffusivity. The Schmidt number of the flow is $Sc = 0.7$. Also the Prandtl number is set to $Pr = 0.7$.

B. LES based on scale selective discretization

Equations (1)–(3) are valid in the limit of DNS where the grid is fine enough to represent all the scales of the flow.¹⁷ In LES, the resolution is coarser than in DNS and Eqs. (1)–(3) are solved for the spatially filtered variables with additional SGS terms appearing as source terms in the equations. In other words, the LES equations¹⁷ can be written in form $NS(\bar{\rho}, \hat{u}_i, \dots) = \tau_{sgs}$. The SGS vector τ_{sgs} requires modeling. Various SGS closure models have been discussed in the literature.¹⁷ Here we choose the scale selective discretization (SSD) approach by Vuorinen *et al.*³⁴ which belongs to the so-called implicit LES (ILES) modeling category^{4,17,27,35–40} with one important difference. In contrast to ILES, the SSD approach targets the dissipative effects only to the smallest scales of a flow via a scale separation procedure. The scale separation is achieved using a Laplacian filter which splits the convection term into low and high frequency parts for which centered and upwind-biased schemes can be separately employed. In the present, unstructured code the SSD scheme is second order accurate. Vuorinen *et al.*³⁴ presented a modified wavenumber (k_{mod}) analysis of the SSD scheme and showed that the SSD scheme is always less dissipative than the standard third order upwind scheme which has been used in previous LES.^{5,35} To summarize, Eqs. (1)–(3) are solved for the grid filtered conservative variables on an unstructured computational grid using centered, second order accurate discretization with SSD scheme applied on the convection term. We set $\tau_{sgs} = 0$ and model the SGS effects by the diffusive truncation error of the SSD scheme which is of third order $\mathcal{O}(\Delta x^3)$. An explicit, density based approach is employed along with the classical 4th-order accurate Runge-Kutta time integration scheme. Among other validation studies (e.g., turbulent channel flow), the solver was validated by Vuorinen *et al.*¹⁶ for turbulent subsonic jets and also laminar flows.

C. Shock capturing

The strong compression effects of the gas are taken into account using a model for the bulk viscosity μ_b which affects the dilational part of the viscous stress tensor in Eq. (6). Here we use the

CC-model by Cook and Cabot²⁸ where μ_b is computed as follows:

$$\mu_b = C_b \rho \Delta^{r+2} |\nabla^r S_{ij}|, \quad r = 2, 4, 6, \dots \quad (9)$$

In Eq. (9) $r = 2$ so that $\nabla^2 S_{ij}$ corresponds to the Laplacian of the rate of strain tensor with a high wavenumber bias. The value $C_b = 5$ is used as recommended in the literature^{5,28,29} and the length scale Δ is computed from a cell volume V_{cell} as $\Delta = V_{cell}^{1/3}$. Fig. 6(d) shows that the bulk viscosity activates at the Mach disk, reflected oblique shocks and along the shear layers of the jet. It is important to note that the influence of μ_b becomes local when it is multiplied with the divergence (flow dilation) (see Eq. (6)). It is known that at a shock position $\|S_{ij}\| \sim |\nabla \cdot \mathbf{u}|$ but in a turbulent flow $\nabla \cdot \mathbf{u} \approx 0$. Thereby, as seen in Eq. (6), μ_b only affects the trace of the stress tensor.²⁸ We note that the range of μ_b is in line with the previous studies.^{5,25}

According to our numerical experiments the CC-model²⁸ as such is not enough for capturing strong normal shocks using FVM since μ_b does not influence the continuity equation. However, Dauphain *et al.*⁵ managed to deal also the normal shocks with the CC-model in LES of supersonic impinging jets since in their simulations the Smagorinsky turbulence model viscosity worked as an adaptive second order filter providing further stabilization at the normal shocks. Here, in addition to the CC-model, we apply a second order filter to the conservative variables locally in the immediate vicinity of the Mach disk at the end of each timestep. The filter is activated in the regions of extreme compressibility using the indicator function of Bhagatwala and Lele²⁹

$$\gamma = \frac{1}{2} (1 - \tanh((0.25 + \frac{\nabla \cdot \mathbf{u}}{c/\Delta})/0.1)), \quad (10)$$

which activates at the location of strong shocks. In Eq. (10) c is the local speed of sound. After $0 \leq \gamma \leq 1$ has been calculated, the local low pass filtering of the conservative variables is carried out at the end of each timestep using a Laplacian filter with coefficient $\gamma \left(\frac{\Delta}{\pi}\right)^2$ which damps the Gibbs oscillation close to the highest wavenumber $k_{max} \approx \frac{\pi}{\Delta}$. Fig. 6(c) shows that γ is non-zero only at the Mach disk vanishing elsewhere. It should be noted that γ is suitable for indicating the normal shock position since $\nabla \cdot (\mathbf{u}\rho) = \rho \nabla \cdot \mathbf{u} + \mathbf{u} \cdot \nabla \rho \approx \rho \nabla \cdot \mathbf{u}$ because the density gradient becomes aligned with the velocity. With these arrangements the simulations become stable, the shock structures become resolved, and the turbulence can be maintained.

D. Simulation setup

In the present study simulations of highly underexpanded jets are carried out in a wall-bounded, closed system as seen in Fig. 2. The system consists of a high-pressure tank at pressure p_o and a low-pressure tank at pressure $p_\infty = 1$ bar. Altogether five simulations are carried out for $p_o = 4.5, 5.5, 6.5, 7.5$, and 8.5 bars. Initially the gas temperature is uniform $T = 293$ K. The two tanks are connected by a converging nozzle and the flow is driven through this nozzle by the pressure gradient. The nozzle exit is located at $z = 0$. Between $-10D < z < 0$ the nozzle does not practically converge anymore and the gas flows through a straight pipe having a diameter $D = 0.0014$ m. The nozzle diameter is the same as in the PLIF experiments¹⁴ but the nozzle pipe itself is only a simplification of the real, converging nozzle. At the nozzle exit, a sonic jet with diameter D is formed with exit velocity $U_1 \approx 330$ m/s and exit Mach number $Ma = 1$. The integral timescale is defined using D and the maximum propagation speed of information at the nozzle exit ($2U_1$) as $T_o = \frac{D}{2U_1} \approx 2.0 \times 10^{-6}$ s. This definition differs from the usual definition by the factor 1/2 but the present choice for the velocity scale also reflects the typical high speed velocities in the near-field of the jet. The total simulation duration is 0.5 ms $= 243T_o$.

The boundary conditions are modeled using the standard Dirichlet-Neumann conditions for the primitive variables p , ρ , T , and u_i . The conservative variables are constructed on the boundary based on the primitive variables. In the low-pressure tank the no-slip boundary condition is enforced for velocity and the walls are set to $T = 293$ K. Inside the nozzle and the high-pressure tank a slip

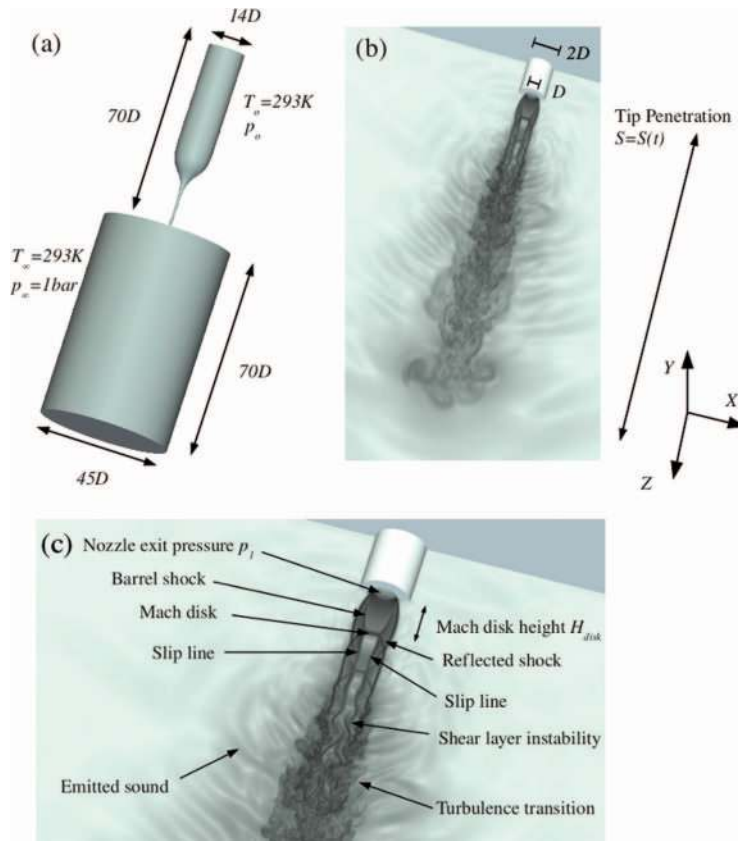


FIG. 2. (a) The simulation geometry shown from the outside. The setup consists of a high-pressure reservoir, a converging nozzle and a large cylinder. (b) An underexpanded jet is formed through a nozzle exit. The nozzle inner and outer diameters are D and $2D$ respectively. (c) The classical picture on shock wave structures in underexpanded jets¹ is reproduced by the present LES.

condition for velocity is employed in order to avoid formation of artificial boundary layers.⁵ Inside the nozzle the zero-gradient condition for temperature needs to be employed due to cooling of the gas while accelerating inside the nozzle. The wall normal gradients of pressure and passive scalar vanish on the walls.

According to previous studies, the spatial resolution in LES of supersonic jet needs to be rather high. Table I gathers some estimates of previously used grid resolutions in the core region of supersonic jets. For example, Dauplain *et al.*⁵ concluded that a resolution of order $D/30$ in the jet core is adequate for obtaining reliable results for a wall impinging jet. Munday *et al.*⁴ used a resolution of order $D/50$ in the cross streamwise direction for a free jet. Rana *et al.*²⁷ applied a resolution of order $D/30$ as well for a jet in supersonic cross flow. The previous studies form a guideline for constructing the present mesh as will be explained in what follows.

TABLE I. Comparison of near-nozzle resolution in present and previous LES of supersonic jets. Resolution is expressed in terms of estimated radial resolution Δr and streamwise resolution Δz .

Author	$\Delta r_{min} \dots \Delta r_{max}$	$\Delta z_{min} \dots \Delta z_{max}$	Cell type	Re
Present study	$D/70 \dots D/50$	$D/35 \dots D/25$	Hexahedral	$\sim 10^5$
Munday <i>et al.</i> ⁴	$D/50 \dots D/35$	$D/50 \dots D/35$	Hexahedral	$\sim 10^6$
Dauplain <i>et al.</i> ⁵	$D/35 \dots D/30$	$D/35 \dots D/30$	Tetrahedral	$\sim 10^6$
Rana <i>et al.</i> ²⁷	$D/33$	$D/33$	Hexahedral	$\sim 2.4 \times 10^4$

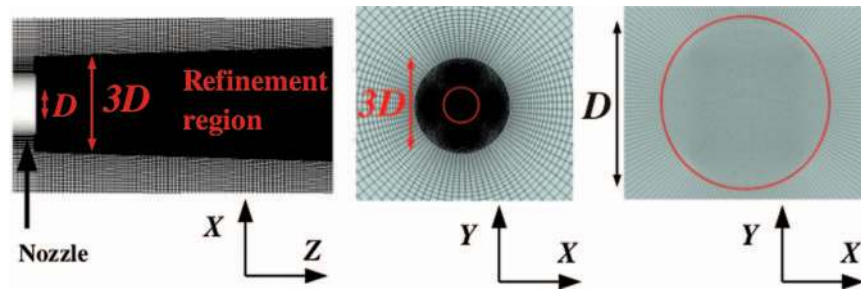


FIG. 3. Grid topology viewed from the cross streamwise and streamwise perspectives. The refinement region extends until $z/D = 22.5$ and it is created into the background grid by splitting the hexahedral cells into 8 parts.

The hexahedral, block-structured grid topology of the present study is presented in Fig. 3. Altogether the mesh contains 12M computational cells. The jet core is meshed with fine resolution by adding a refinement region which covers the jet core and the developing shear layers. The refinement region extends until $z/D = 22.5$ thereby covering the main region of interest in this study. Inside the refinement region the hexahedral cells of the background mesh are split into 8 parts. Despite slight stretching of the grid, the present mesh allows good control over the grid quality and the control volume dimensions are typically always within $D/35 \leq \Delta z \leq D/25$ in the streamwise and $D/70 \leq \Delta r \leq D/50$ in the cross streamwise directions within the region of interest. Note that $\Delta z = D/35$ until $z/D = 12$ covering the transitional region where we carry out for example the POD analysis. After $z/D = 22.5$ the background resolution is recovered and the grid stretching becomes more pronounced in order to damp the downstream propagating waves before they interact with the bottom wall of the cylinder which is located at $z/D = 70$. With these arrangements the resolution requirements presented in the previous studies^{4,5,27} are met in large portion of the jet core region.

E. Initial conditions and flow rate in highly underexpanded conditions

Yu *et al.*¹³ have explained the flow development stages in highly underexpanded jets: (1) initial delay time due to opening of the solenoid valve or injector needle, (2) flow development in the nozzle and building up of the pressure gradient in the nozzle, and (3) fully developed flow. In particular, stage 2 influences the nozzle exit pressure p_1 and it is usual to observe all the standard jet conditions in practice including subsonic, moderately underexpanded and highly underexpanded flow.¹⁴ In DI NG-engines the development times can be comparable to the total injection duration (~ 1 ms)^{10–14} due to the delay in opening of the injector needle and rather large physical size of typical injectors in comparison to the nozzle diameters.

In the present paper, the simulation is considered to begin from the end part of stage 2. Since the pressure profile at that stage is unknown, it has to be modeled. We initialize the pressure field using a hyperbolic tangent function which varies smoothly from value p_o to p_1 at the nozzle exit, see Fig. 4. At $t = 0$ we set $p_1 > p_\infty$ to allow fast jet development. The pressure in the chamber is set to $p_\infty = 1$ bar. In the fully developed state, $p_1 > 2$ since the jet is highly underexpanded¹ and the flow is not assumed to be dependent on the initial condition anymore. It is considered important, that the nozzle exit pressure p_1 builds up solely due to the nozzle flow and, for example, linking p_o and p_1 with analytical relationships is avoided. At the start of injection (SOI) the upstream traveling expansion wave is noted in Fig. 4. Around time $t = 90T_o$ the system has reached a steady state which can be seen from the pressure profiles and steady mass flow which is noted to vary linearly with the nozzle pressure ratio.

III. RESULTS

A. Steady state jets

First, we present visualization of the instantaneous jets in steady state conditions by considering the contour plots of $\log_{10}(|\nabla \rho|)$. Fig. 5 shows how NPR affects the shock cell patterns. The present

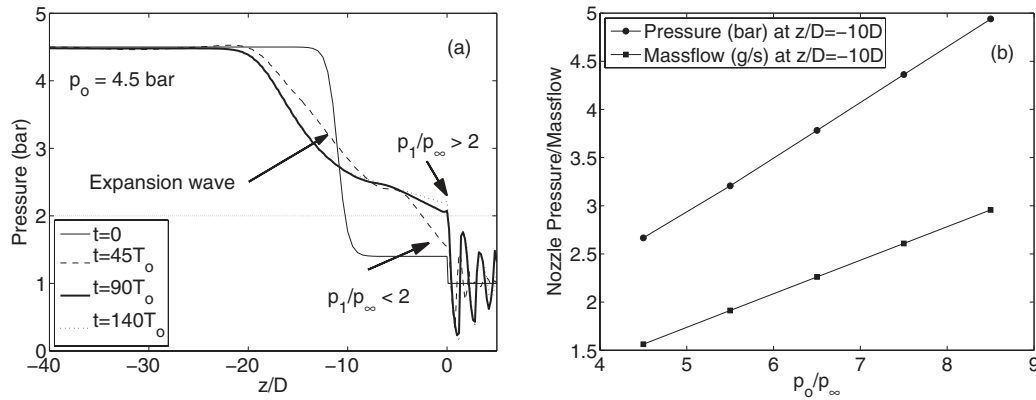


FIG. 4. (a) Time development of pressure profile along the z -axis. The steady state is reached by $t \approx 90T_0$. (b) The steady state nozzle pressure and mass flow rate at the monitoring point $z/D = -10$ located on the jet axis are confirmed to scale linearly with p_0/p_∞ .

jets feature a barrel shock terminating at a first normal shock, the Mach disk, in the near nozzle region $z/D < 3$. The parallel slip lines start from the Mach disk and they continue until turbulence develops in the shear layers via growing instabilities which eventually reach the jet core between $4.5 \leq z/D \leq 7$ depending on NPR . In between the slip lines a train of shock cells forms due to reflection of shocks from the shear layers of the jet. Similarities between the present visualization and previous experimental Schlieren experiments^{1,4,6,7,12,13} arise, in particular, from the viewpoint of shock structure- NPR dependency. To our knowledge the effect of NPR on jet structure has not been systematically studied by LES previously but, nevertheless, the present LES compares favorably with the previous “numerical Schlieren” visualization by Munday *et al.*⁴ and Dauplain *et al.*⁵ in terms of shock patterns (reflection, slip line position, shock cells after the Mach disk). In particular, it is very clear that the height (H_{disk}) and the width (W_{disk}) of the Mach disk increase with increasing NPR as seen in Fig. 5. Also, the jet tip penetration and the jet volume increase with increasing NPR .

In the present LES turbulence starts to develop after the Mach disk and we observe no flow outside the first shock cell. Potentially, it would be possible to observe Görtler vortices (GVs) outside

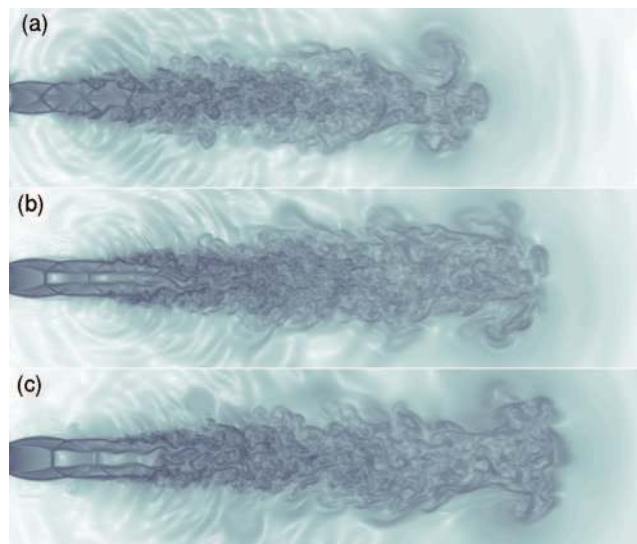


FIG. 5. Density gradient ($\log_{10}(|\nabla \rho|)$) at time $T_0 = 90$ for (a) $p_0/p_\infty = 4.5$, (b) $p_0/p_\infty = 6.5$, and (c) $p_0/p_\infty = 8.5$. The size of the view extends to $z/D = 25$.

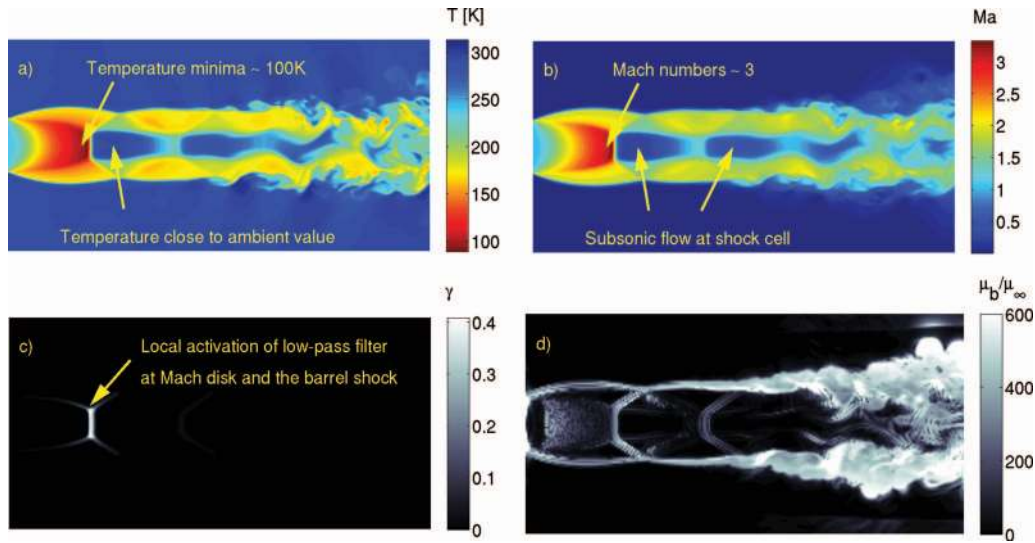


FIG. 6. Instantaneous snapshots of various flow quantities for $p_0/p_\infty = 6.5$. (a) Temperature, (b) Mach number, (c) the strong shock sensor (γ), and (d) CC bulk viscosity (μ_b/μ_∞).

the first cell if the Görtler number (G) exceeds 0.3 ($G = \frac{U\theta}{\nu} \left(\frac{\theta}{R} \right)^{1/2}$, where U = velocity scale, θ = incoming boundary layer thickness, ν = kinematic viscosity, and R = radius of curvature of the shock cell boundary).⁴⁸ Here the onset of the instability depends mostly on θ and R . For example, Dauplain *et al.*⁵ have reported LES where GVs were observed outside the barrel shock. The LES by Dauplain *et al.* posed several sources of asymmetry (tetrahedral grid and wall-jet interactions) which could rapidly trigger the GVs. Here, the grid is very symmetric and the instability is likely to grow slower. In fact, literature has shown that development of the gas motion outside the barrel shock and jet boundary when $z/D < 3$ depends on the nozzle configuration (e.g., possible asymmetries) and on the level of turbulence development at the nozzle exit.^{1,4,6,7,12,13} For example, Panda *et al.*⁷ and Munday *et al.*⁴ have reported experiments where almost no visible turbulence was observed at the boundary or outside the barrel shock. We conclude that in reality the growth rate of Görtler instabilities is likely to depend on the turbulence development at the nozzle exit.

Fig. 6 demonstrates the spatial variation of the gas temperature, Mach number, artificial bulk viscosity (μ_b) and the normal shock sensor (γ) in the fully developed state. In the near nozzle region the jet is characterized by the barrel shock and the Mach disk. At the nozzle exit the flow velocities are very close to sonic velocities ($Ma \approx 1$). The very rapid expansion leads to high Mach numbers close to 3 in the vicinity of the Mach disk. At the barrel shock position the flow compresses which increases the gas density and concentration. The Mach disk itself is characterized by temperature minima and discontinuity in the primitive variables.⁵ It is observed that the gas undergoes strong cooling by factor 0.3 from the reservoir temperature levels leading to temperatures of order 100 K at the Mach disk. Immediately after the Mach disk the flow becomes again subsonic as expected.¹ The subsonic regions are seen to occur in the shock cells where the thermodynamic conditions are close to the ambient values $T_\infty, p_\infty, \rho_\infty$. The panel (c) of Fig. 6 shows how the indicator function γ (Eq. (10)) activates the low pass filter only in the immediate vicinity of the normal shock. The activation of the bulk viscosity (Eq. (9)) is noted at the shocks and the jet shear layers as anticipated based on previous studies^{5,29}

B. Volumetric growth

The jet tip penetration $S(t)$ is a very important property of fuel jets since it determines also the volumetric growth rate of the jet. The volumetric growth can be further linked to mixing and entrainment which are two vital processes for fuel jets influencing the level of emissions in chemically reacting flow. For underexpanded sonic jets Ouellette and Hill¹¹ have found that $S/(\rho_0/\rho_\infty)^{1/4} \sim t^{1/2}$.

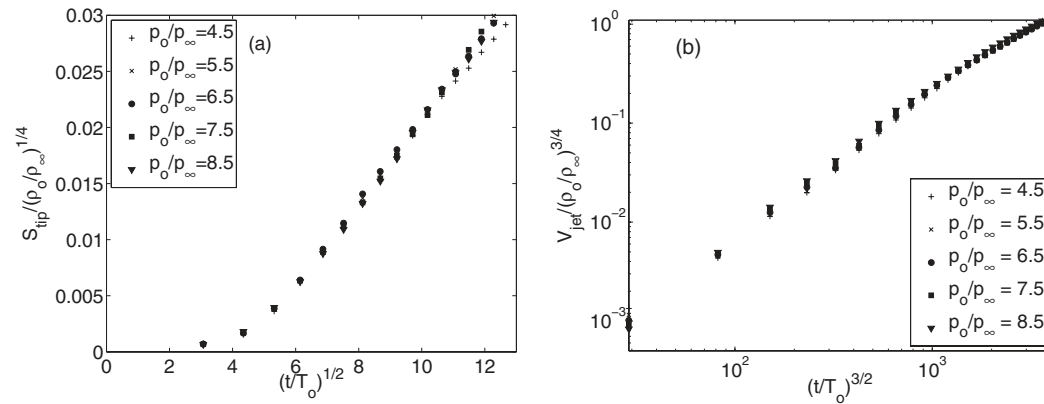


FIG. 7. (a) Tip penetration of the jet. (b) In normalized variables the data collapses onto a single line.

The present LES, see Fig. 7(a), clearly confirms this behavior after the initial transients have passed by and the pressure gradient has fully developed across the nozzle for the jet to be underexpanded. The link between the tip penetration and jet volume has been given little attention in the literature. Experimental measurement of jet volume is difficult since the data are typically 2d. Yet, in LES the jet volume can be evaluated from 3d data. Here, we define the jet volume as the set of cells where the concentration exceeds the threshold value $\rho c = 0.001$, that is, $V(t) = \int_{\rho c > 0.001} \delta V$. From the cone-like geometry of the jets it is anticipated that $V \sim S^3 \sim t^{3/2}$ if S is taken to be the “height” of the cone and the “tip” of the cone is located at $z = 0$. Indeed, Fig. 7 confirms that the jet volume scales quite well with $t^{3/2}$. After normalization a data collapse is noted implying a $V/(\rho_o/\rho_\infty)^{3/4} \sim t^{3/2}$ scaling for the volumetric jet growth. This will be further discussed in the end of the paper.

C. Development of the shock cells

We investigate the early stage of the jet injection, focusing on the density history and shock establishment. This information is not accessible using experimental techniques. Fig. 8 shows transient formation of a jet at injection pressure $p_o/p_\infty = 6.5$. At an early time $t = 14T_o$ a tip-vortex characteristic to subsonic jets is observed (a). Soon, at time $t = 18T_o$, the Prandtl-Meyer expansion

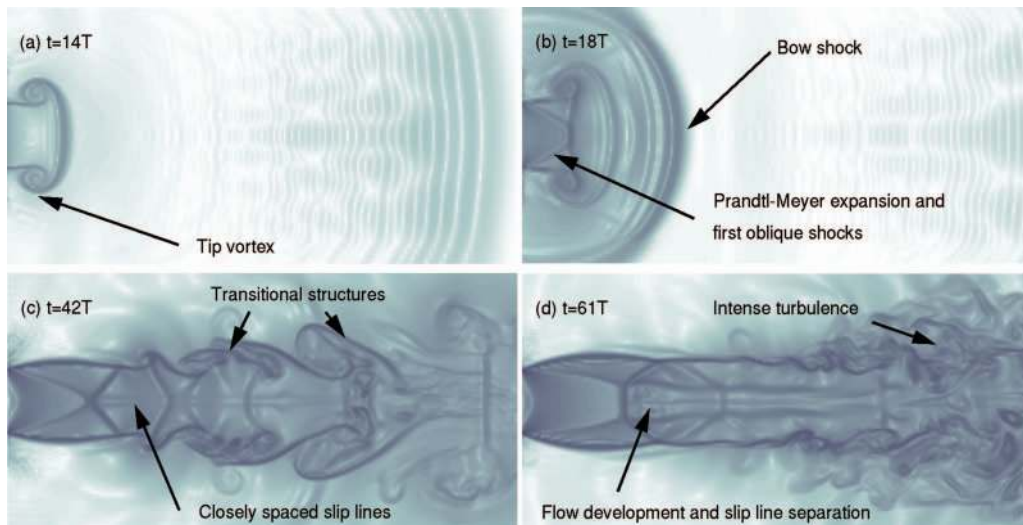


FIG. 8. A close-up to the nozzle exit showing how an initially subsonic jet (a) turns its character in the Prandtl-Meyer expansion around time $t = 16 - 18T_o$ (b). The process is followed by growth of the Mach disk (c) and (d).

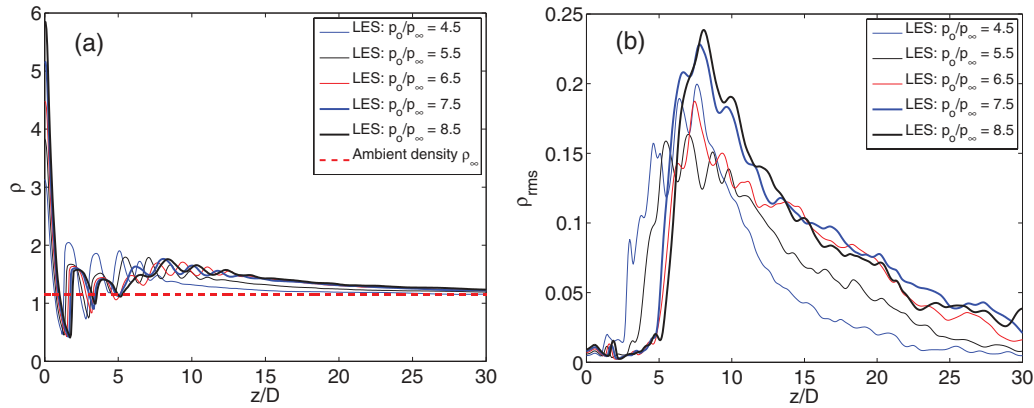


FIG. 9. (a) Axial density ($[\rho] = \text{kg/m}^3$). (b) Axial RMS density ($[\rho_{rms}] = \text{kg/m}^3$).

leads to formation of spherically propagating bow shock followed by the development of oblique shocks (diamond shocks) near the nozzle exit. When the nozzle exit pressure p_1 has increased above the threshold level for highly underexpanded flow ($p_1 = 2p_\infty$), the Mach disk begins to develop.¹ For $NPR = 6.5$, p_1 exceeds 2 when $t = 40 - 50T_o$. Fig. 4 shows that for $NPR = 4.5$ the flow develops almost as quickly as for $NPR = 6.5$ but p_1 exceeds p_∞ only slightly since the $NPR = 4.5$ case is almost at the limit of highly underexpanded flow. Typically, in all the studied cases the Mach disk is initially very narrow but in $10 - 20T_o$ the slip lines become more separated from one another as the disk width grows. Based on Fig. 8 these stages take altogether about $50 - 70T_o$ after which the Mach disk is fully developed.

The shock cells can be observed from a plot of axial density profiles as seen in Fig. 9(a). The density decreases sharply from the high nozzle exit value, oscillates around a low level, increases to a maximum at $z/D \sim 8$ and decreases asymptotically towards ρ_∞ . The lower the NPR the faster the rate of decay. For the highest NPR the axial density is still about 10% above ρ_∞ at $z/D = 25$. Also the axial density fluctuations show interesting behavior as noted in Fig. 9(b). The density fluctuations peak around $z/D \sim 7-10$ after which the fluctuations decay slowly towards zero. The peak is shifted more downstream with increasing NPR since the turbulence transition process is slower for higher NPR . The peak location occurs after the shear layers have reached the jet axis. In absolute (and also normalized) terms the peak of ρ_{rms} is the highest for the highest NPR . The large density variations imply high compressibility effects until at least $z/D = 30$.

Fig. 10 shows the time development of axial density for $NPR = 4.5$ and 6.5 . The diagram of Fig. 10 is constructed by plotting the axial density profiles as a function of time in $(z/D, t/T_o)$ -plane. A line pattern (I) appears at $t = 0$ corresponding to a very weak, hardly visible initial pressure

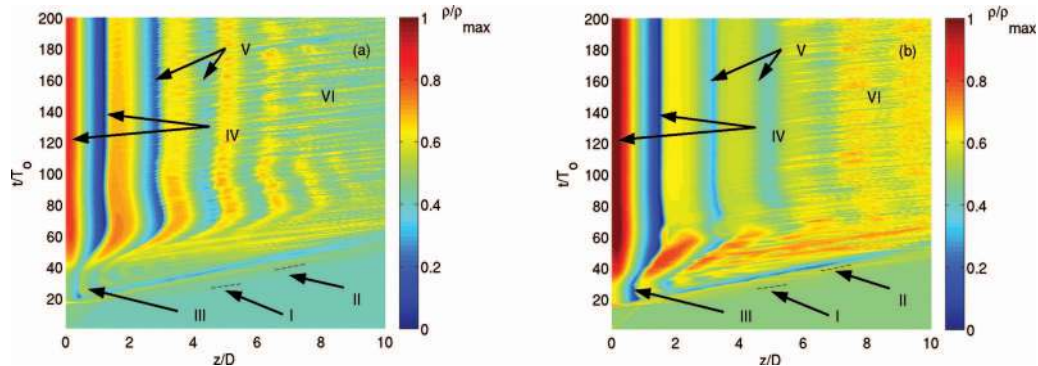


FIG. 10. Phase portrait of normalized density (ρ/ρ_{max}) along the z -axis in $(z/D, t/T_o)$ -plane. (a) $NPR = 4.5$ and (b) $NPR = 6.5$. The dashed lines work as a guide to the eye for pointing out wave propagation speed.

wave that originates from the nozzle and propagates at the speed of sound (U_1). A clear line pattern (II) is noted for all NPR starting from $z/D = 0$ at time $t \approx 17T_o$. It features a local pressure peak followed by a pressure minimum corresponding to the bow shock in Fig. 8. The bow shock moves at velocity $0.6U_1$. After passage of the bow shock, density gradients form in region III while the jet undergoes the Prandtl-Meyer expansion. From Fig. 8(c), it is seen that this transition corresponds to a cone shaped shock cell evolving towards the Mach disk. At the stabilization time, it consists of a region of high density downstream of the nozzle followed by a smooth density decrease (over $2D$) ended by a sudden increase. This feature is highlighted as region IV and corresponds to the part starting at the nozzle and extending up to the Mach disk. In region III a faint density minimum is noted for $NPR = 4.5$ which moves downstream and becomes stronger in region IV around time $t/T_o = 60$. For $NPR = 6.5$ the similar minimum is stronger in region III and it moves downstream to region IV without changing its intensity. This indicates more rapid establishment of the Mach disk for higher NPR . Further downstream of the Mach disk, two diamond shapes cells (region V) are seen but not appearing before $t = 75T_o$. After that, a collection of periodic, horizontal lines are noted in region VI.

D. Time averaged concentration and velocity fields

The cross-sectional concentration field images from LES are next compared with their experimental counterparts based on the PLIF technique. The present measurements have been described in detail in the previous work by Yu *et al.*^{13,14} In the present PLIF, nitrogen jets are injected into ambient conditions with various injection pressures. Acetone vapor is used as a fluorescent tracer. PLIF is well suited for flow visualization with the particular advantage of offering cross-sectional information of the jets. PLIF has been previously used to gain further confidence to LES by various authors.^{25,27}

In PLIF significant pressure losses occur inside the nozzle.^{13,14} Therefore, the LES and PLIF need to be compared by choosing cases where the Mach disk heights are similar and the experimental jets can be considered to be operated at the same effective NPR as the present LES. Based on Fig. 11 the average ρc distribution of the present LES compares well with the structures obtained in PLIF. In particular, the region $z/D < 5$ is qualitatively well captured. Also the observed number of shock cells in LES and PLIF is the same. The jets pose strong localization of mass and concentration in the co-annular shear layers of the jet. Fig. 12 shows that increased ρc implies the momentum to be channeled into the annular shear layers. For example, after the Mach disk, when $z/D < 10$ supersonic velocities are noted in the shear layers whereas the shock cell centers correspond to the low speed subsonic regions where the stagnation conditions are met. The axial mean velocities reach supersonic values until $z/D = 20$. Also the jet core is long in contrast to subsonic jets where the potential core length is typically $4 - 6D$. The shock cell pattern dictates the velocity relaxation until $z/D \sim 10-14$.

The highest NPR shows a clear inner and a clear outer shear-layer as seen from Figs. 11 and 12. The shear-layers extend downstream more and more when increasing NPR . Fig. 12 shows that also the RMS of velocity has high values in the shear layer. The RMS also shows a clear influence of the NPR on the fluctuation pattern. At low NPR , the two peak RMS or shear-layers merge at $z/D = 10$ while they extend much longer for the other cases. For instance at high NPR , the RMS level remains large at $z/D = 20$ while it has already decreased for low NPR . The peak of ρ_{rms} around $z/D \sim 8$ in Fig. 9 is related to Fig. 12 and the collapse of the annular jet in the respective location. The structure of the shear layer will be further analyzed with POD in the end of the paper.

One primary difference between the present PLIF and LES is that turbulence is observed outside the barrel shock in PLIF in contrast to LES. Additionally, the experimental jet shear layers develop faster than those in LES. This difference is understandable due to differences in the setups. For example, in LES the nozzle wall boundary layers and turbulence are not modeled and we use the slip velocity boundary condition inside the nozzle. This explains already most of the discrepancies between LES and PLIF since in the experiments the nozzle flow probably poses turbulent boundary layers. The experimental jets have also developed for several milliseconds and thereby the turbulence had time to develop. In the experiments, also the injector poses some asymmetric features which

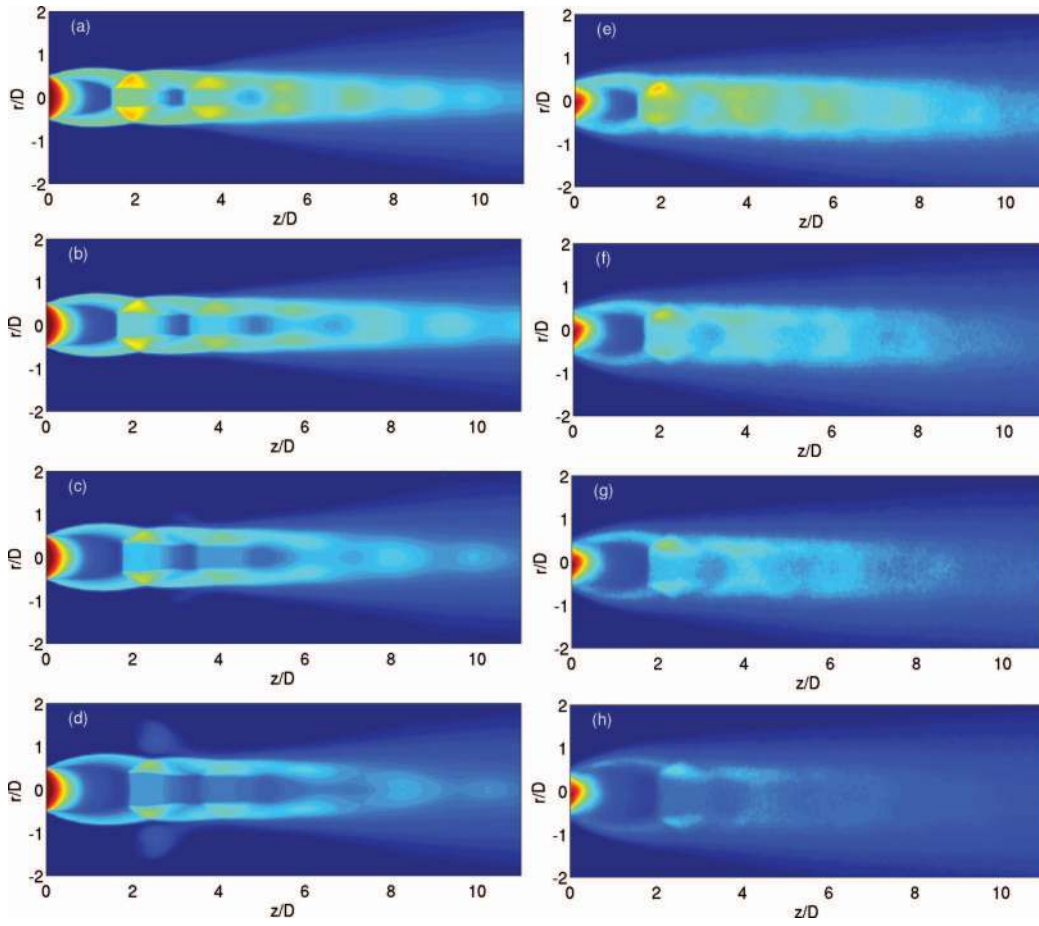


FIG. 11. Average concentration (ρc) and a comparison of LES (a)–(d) and PLIF (e)–(h). (a) $p_o/p_\infty = 5.5$, (b) $p_o/p_\infty = 6.5$, (c) $p_o/p_\infty = 7.5$, and (d) $p_o/p_\infty = 8.5$.

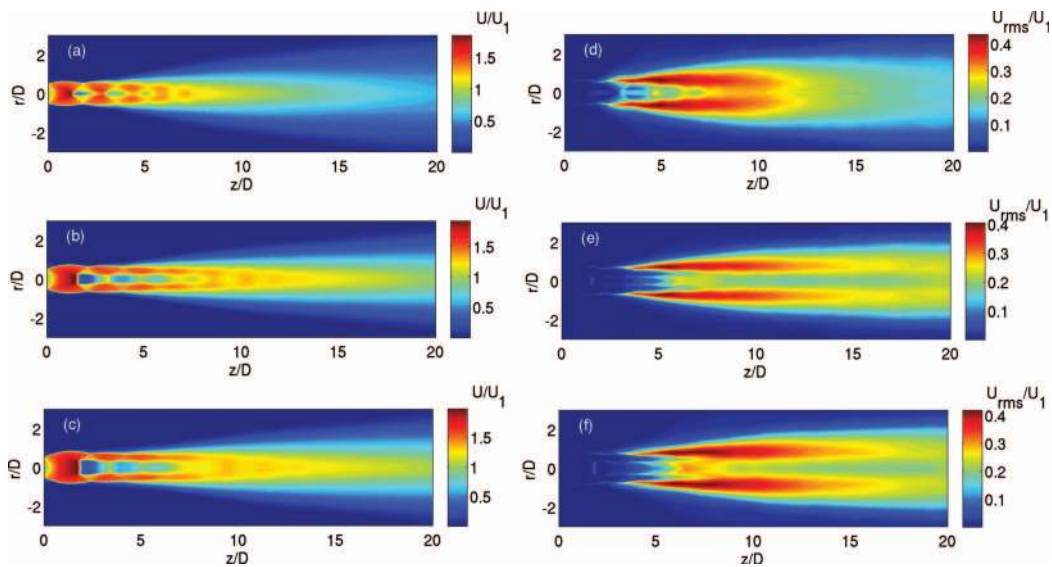


FIG. 12. Velocity statistics from LES. Average streamwise velocity (a)–(c) and RMS velocity (d)–(f) normalized by nozzle exit velocity ($U_1 \approx 330$ m/s). ((a) and (d)) $p_o/p_\infty = 4.5$, ((b) and (e)) $p_o/p_\infty = 6.5$, and ((c) and (f)) $p_o/p_\infty = 8.5$.

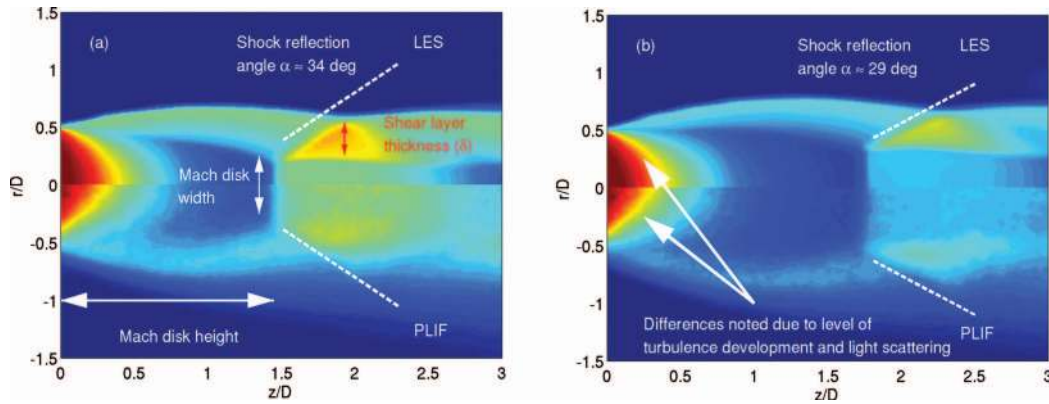


FIG. 13. Comparison between concentration fields obtained from LES (upper half) and PLIF (lower half). Also the shear layer thickness (δ) and the shock reflection angle (α) are defined. (a) $p_o/p_\infty = 5.5$ and (b) $p_o/p_\infty = 7.5$.

produces clearly noticeable deviation from symmetry in reality. The same explanation holds true further downstream where differences in the shock cell structures are observed.

E. The Mach disk

Fig. 13 shows a close-up to the jet inlet. As can be seen, PLIF and LES both show how the injection pressure influences the Mach disk height (H_{disk}) and width (W_{disk}). In particular, W_{disk} determines also the separation between the slip lines and it thereby has an integral role in the formation of the annular shear layers. As can be seen from Fig. 13, shocks are reflected from the triple point located at the edge of the Mach disk. The triple point (see Fig. 1) is the intersection point of the barrel shock, the Mach disk and the first reflected shock. The angle of the first reflection (α) is affected by NPR so that α decreases with increasing NPR . For $NPR = 5.5$ we measure $\alpha \approx 34^\circ$ whereas for $NPR = 7.5$ the value $\alpha \approx 29^\circ$ is observed. Both angles are close to the estimated values measured with PLIF. We also note that the thickness of the shear layer (δ) varies with NPR so that $\delta \approx 0.44D$ for $NPR = 4.5$ but falls to approximately a constant value $\delta \approx 0.35D$ for $NPR \geq 5.5$. The reflection angles as well as the shear layer thickness for all NPR are tabulated in Table II.

The height of the Mach disk H_{disk} increases as a function of the injection pressure. Ashkenaz and Sherman⁴⁵ have derived the following formula for the NPR - H_{disk} relationship:

$$H_{disk}/D = C \sqrt{\frac{p_o}{p_\infty}}. \quad (11)$$

The derivation by Ashkenaz and Sherman⁴⁵ leads to the constant $C = 0.67$. The result seems to be valid only for higher injection pressures since for $NPR < 10$ Ewan and Moodie⁴⁶ observed experimentally a smaller value $C \approx 0.55$ but with C approaching 0.67 with increasing NPR . The

TABLE II. Summary of results for highly underexpanded jets. Frequencies expressed as Strouhal number ($St = fD/2U_1$), length scales normalized with D and the shock reflection angles expressed in degrees. E_{peak}/E_{tot} denotes the fraction of sound energy contained in the dominant pressure fluctuation peak.

p_o/p_∞	H_{disk}	W_{disk}	δ_{shear}	α_{shock}	$f_{peak}(p')$	$f_{peak}(a_1(t))$	$E_{peak}/E_{tot}(p')$
4.5	1.30	0.14	0.44	40.3	0.463	0.168	10.1%
5.5	1.43	0.36	0.36	34.2	0.462	0.462	7.1%
6.5	1.59	0.46	0.35	31.2	0.388	0.388	3.1%
7.5	1.72	0.55	0.35	29.3	0.381	0.381	5.9%
8.5	1.84	0.68	0.35	28.5	0.368	0.368	6.4%

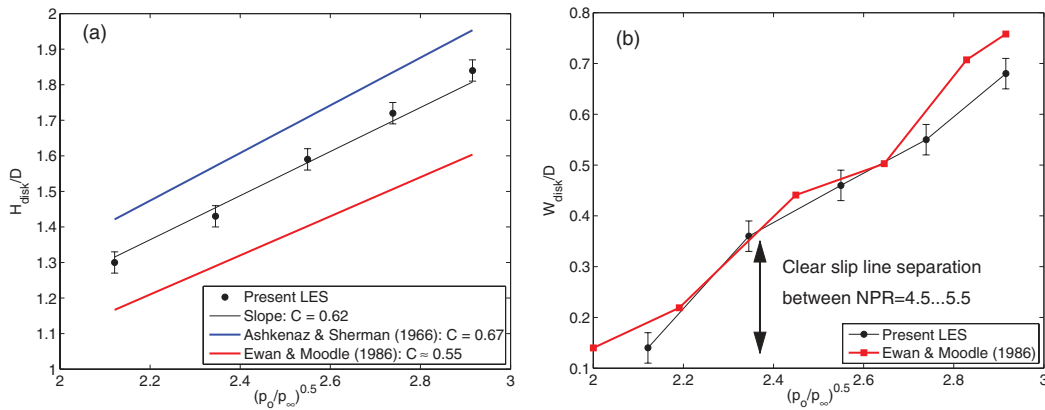


FIG. 14. (a) Dependence of the Mach disk height on the pressure ratio p_o/p_∞ . (b) Dependence of the Mach disk width on the pressure ratio p_o/p_∞ .

validity of Eq. (11) is investigated in Fig. 14. It is seen that the present LES produces an approximate slope 0.62 which is in between the earlier predictions.^{45,46} Ewan and Moodie have also investigated W_{disk} and noted that at low NPR the Mach disk width scales with $W_{disk}/D = C_w \sqrt{p_o/p_\infty}$ where C_w is a strong function of NPR .⁴⁶ A major observation is that the slip lines are very close to each other for $NPR = 4.5$ but they become strongly separated when NPR increases to $NPR = 5.5$. Simultaneously with increasing W_{disk} , the shear layer thickness δ and the angle α decrease. Thereby, the jet strongly changes its character around $NPR = 5$ into a co-annular jet. The values of H_{disk} and W_{disk} are also tabulated in Table II.

F. Mixture quality

Two matters need to be distinguished from each other: (1) injection of a real fuel (e.g., natural gas) and (2) injection of a passive scalar. First, in a “real” DI NG engine a higher nozzle pressure ratio can produce a richer mixture on average. A way to argue this is discussed below. We showed previously that, in line with previous studies, the jet volume evolves as $V(t) \sim (\rho_o/\rho_\infty)^{3/4} t^{3/2}$. On the other hand, the mass flow scales linearly with NPR , i.e., $\dot{m} \sim \rho_o/\rho_\infty \sim p_o/p_\infty$ (see Fig. 4). The analysis leads to the conclusion that the global average mixture level $c_{ave} \sim (\rho_o/\rho_\infty)^{1-3/4} \sim (\rho_o/\rho_\infty)^{1/4}$ indicating that the average concentration levels stay higher when the NPR is higher. However, the scaling exponent $1/4$ is small and, in practical situations with rather narrow pressure operating conditions, the given analysis implies that NPR has little effect on the mixture richness due to the favorable scaling of jet volume with exponent $3/4$.

In the present LES mixing of a passive scalar is simulated instead of NG. The injection rate of ρc is kept constant. In fact, this situation is also similar to the PLIF measurements.^{13,14} It is expected that in such a configuration higher NPR leads to faster mixing of the scalar since the jet penetrates also faster. In PLIF this is seen as weaker signal levels at high NPR despite the fact that approximately the same amount of acetone enters the chamber. The global probability density function (PDF) of ρc over the whole jet volume ($\rho c > 0.001$) shows the better mixing as seen in Fig. 15. It is noted that when time proceeds the higher NPR leads to lower concentrations thanks to rapid volumetric growth. At low NPR the flatter peaks are related to unmixingness and lower RMS. The peak location gives an idea of how much gas/air has entrained while the peak height relates to the mixing between the jet and the entrained volume. As is seen, the high NPR have both a higher and narrower peak so both the entrainment and the mixing are better.

G. Proper orthogonal decomposition

In proper orthogonal decomposition (POD) the aim is to project the turbulent flow field on basis functions that maximize the turbulent kinetic energy content for any subset of the base.^{41–44} The

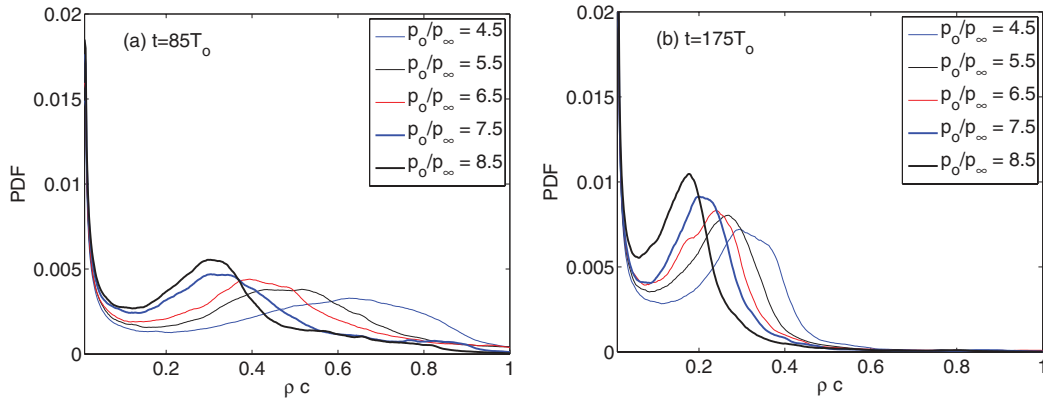


FIG. 15. Time evolution of the probability density of ρc . It is observed that for all times the higher the NPR, the lower the concentration levels and the better the mixing.

pioneering work on applying POD on turbulent data was carried out by Lumley.⁴² Next, we apply POD on LES data^{41–44} to extract information on the coherent flow structures. We apply the POD method of snapshots by Sirovich⁴³ in which time snapshots $(\rho, \rho u, \rho v, \rho w)_s$, $s = 1, \dots, N$, where N = number of snapshots are made zero-mean by subtracting the average and also normalized with ρ_∞ and U_1 . Here, the snapshots are 2d cutplanes of the 3d flow field. After normalization, the snapshots are collected as the columns of the snapshot matrix M . The eigenvalue analysis of the autocovariance matrix $C = M^T M$ results in the construction of a basis $\{\psi_s\}_{s=1}^N = \{(\varphi_\rho^s, \varphi_{\rho u}^s, \varphi_{\rho v}^s, \varphi_{\rho w}^s)\}_{s=1}^N$ which is arranged in the decreasing order of eigenvalues of C so that $\lambda_1 \geq \lambda_2 \geq \dots \geq \lambda_N$. Any snapshot can be expressed as

$$(\rho, \rho u, \rho v, \rho w) = \sum_{i=1}^N a_i(t) \psi_i, \quad (12)$$

where the time coefficients $a_i(t)$ are computed as inner products (projections) between the snapshot and the basis function.^{43,47} The orthogonal modes correspond to the energetic, coherent flow structures and they are used to extract deterministic features from turbulent data.

Figs. 16(a), 16(c), and 16(d) present mode 1 for three NPRs. For reasons to be explained later, mode 2 would look visually the same as mode 1 but it would pose a spatial phase shift to ensure

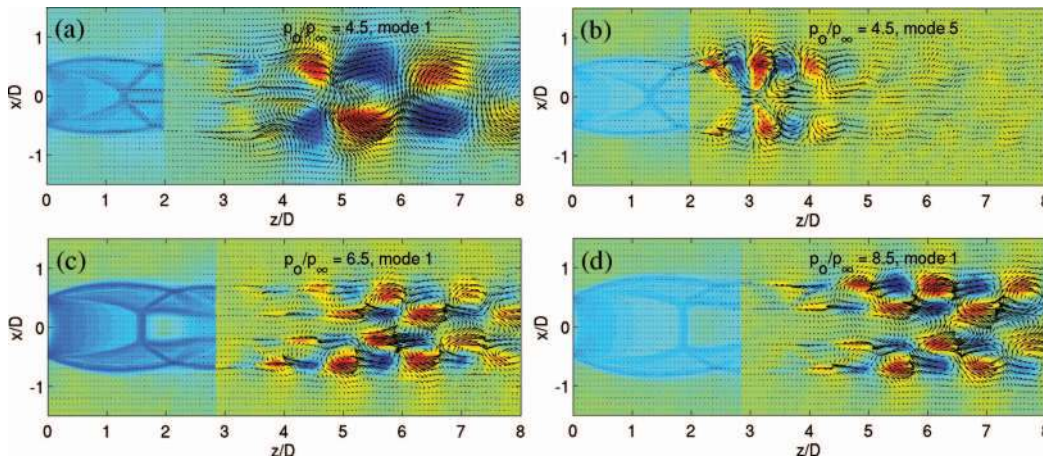


FIG. 16. The shock structures shown together with the non-vanishing part of the density mode (φ_ρ) superposed with the velocity vectors of the momentum mode ($\varphi_{\rho u}, \varphi_{\rho v}$). (a) $p_0/p_\infty = 4.5$, mode 1, (b) $p_0/p_\infty = 4.5$, mode 5, (c) $p_0/p_\infty = 6.5$, mode 1, and (d) $p_0/p_\infty = 8.5$, mode 1.

orthogonality between modes 1 and 2. In addition to mode 1, Fig. 16(b) also presents mode 5 for $NPR = 4.5$. We show the modes after the Mach disk only, since the related modes vanish near the nozzle exit where the variance content is very small as seen also from the RMS of velocity in Fig. 12. Instead, this part is replaced with the first shock cell in order to better relate the mode location with the shock structures. As is seen in Fig. 16, increasing the NPR changes the shape and extent of the modes. At $NPR = 4.5$, mode 1 shows anti-symmetric alternating pockets of positive and negative density fluctuations. As the vectors show, these structures correspond to a collection of aligned vortices: any vortex is a counter-rotation with respect to the previous or the following vortex. The observed vortex size is approximately D . The vortices are positioned within the slip lines explaining the vortex dimension. For $NPR = 4.5$, mode 5 shows a similar pattern but the wavelength is shorter.

Previously it was shown that increasing NPR channels momentum to the shear layer which gives the jets a co-annular character. As is seen in Fig. 16, also the dominant mode changes shape: small vortex structures appear in the inner and outer shear layers. The axial wavelength of repeating pattern decreases to $\sim D$ and the vortex size becomes $\sim D/2$. For $NPR = 6.5$ and 8.5 , the modes look similar but they start further downstream with increasing NPR ($z/D \sim 4$ at $NPR = 8.5$ compared to $z/D \sim 3.5$ at $NPR = 6.5$). At $NPR = 6.5$ and 8.5 , the dominant mode is concentrated in the annular jet created by the slip lines until the opposite sides of the jet meet on z -axis. For all NPR , the development of the dominant mode is constrained by the flow topology. The location of the shear-layer, as seen in Fig. 16, influences the mode shape and associated vortex size and location. In general, the results indicate that for all the NPR mode 1 begins after the second normal shock (Mach disk being the first normal shock).

Fig. 19(a) shows the POD eigenvalue spectrum ($\lambda_i/\sum_j \lambda_j$) for different NPR . Modes 1 and 2 cover about 6%–12% of the variance content and it is noted that λ_1 is very close to λ_2 . Visual inspection of modes 1 and 2 confirms that they look structurally very similar and pose the same spatial wavelength. However, a spatial phase shift is observed ensuring orthogonality between the modes. The presence of mode pairs is common in swirling flows and they can be related to a rotational flow component.³⁶ Mode pairs were also reported for systems without swirl^{36,47} but without lower relative intensity (in terms of fraction of variance covered by the pair alone). The fraction of variance covered by mode pair (1,2) is function of the NPR with higher NPR exhibiting about 10%–12% of the variance of the variable vector. As can be seen from Fig. 17(b), the variance distribution is relatively flat unlike in swirling flows. In fact with the present sampling ensembles, about 50 modes are needed to reproduce 50% of the variance. Subsequent modes of the pair (1,2) may also present a defined coherent structure and appear as a pair, e.g., modes 5 and 6 at $NPR = 4.5$ and 8.5 . However, they contain a smaller fraction of the variance.

Next, the time variation of the POD modes is analyzed. Fig. 18(a) shows the time coefficients indicating that $a_1(t)$ and $a_2(t)$ are harmonic functions with a phase shift. Both have the

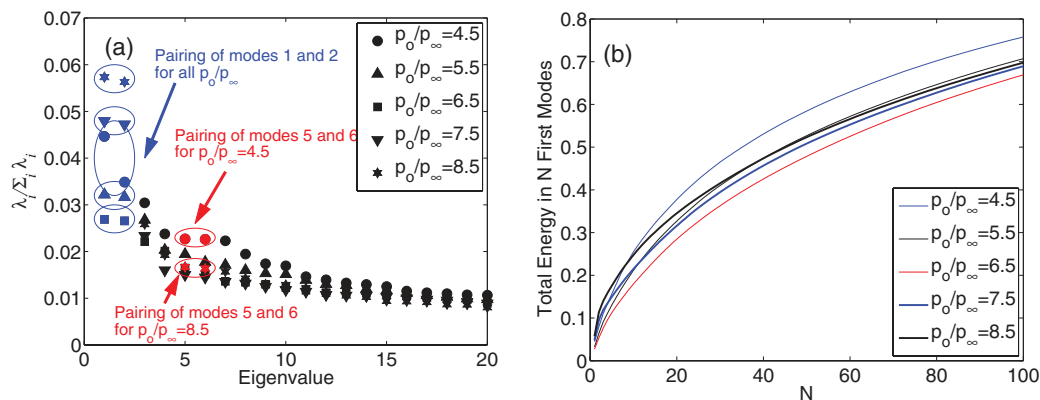


FIG. 17. (a) POD eigenvalue spectrum. (b) Cumulative energy in the first N POD modes.

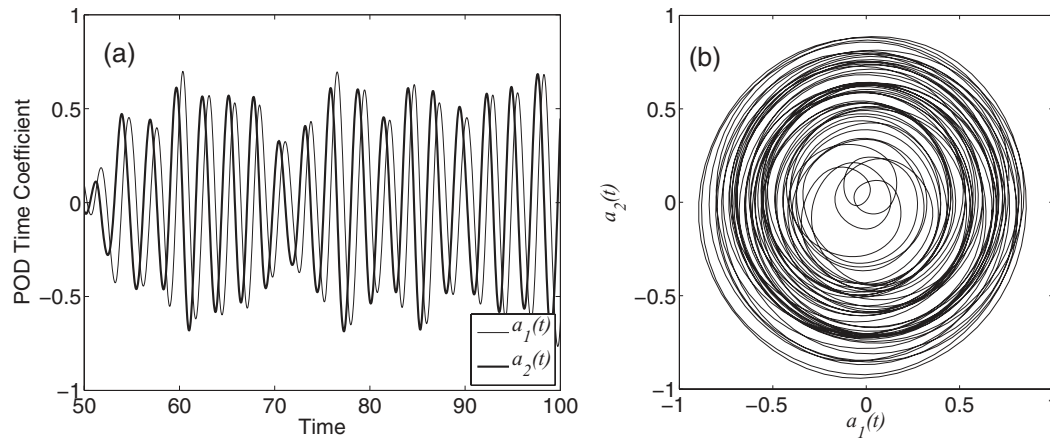


FIG. 18. (a) POD time coefficients $a_1(t)$ and $a_2(t)$ showing the coupling between mode pair (1, 2) for $p_o/p_\infty = 8.5$. (b) Plot of $a_1(t)$ vs $a_2(t)$ revealing the pairing for $p_o/p_\infty = 8.5$.

same characteristic frequency and they undergo the same amplitude modulation. Lissajous' plot in Fig. 18(b) indicates circular trajectory giving a phase shift of $\pi/2$. The same observation holds true for all the mode pairs (1,2) in the investigated *NPR* range. The temporal phase shift ensures orthogonality of the time terms and is common for POD modes that appear in pairs.^{36,37} In Fig. 19, frequency analysis in Fourier space is carried out. In line with the definition of the integral timescale, frequencies are normalized by $1/T_o$ and the Strouhal number is defined as $St = fD/2U_1$. This definition is directly linked to the standard definition of Strouhal number by the factor 1/2 due to different definition of the characteristic velocity. In Fig. 19(a) the POD time coefficients evidence characteristic frequencies as distinct peaks as expected also from Fig. 18. Fig. 19(b) reveals similar peaks in the spectrum of pressure fluctuation probed at $z/D = 10$, $r/D = 3$ in the far field of the jet. To complement Fig. 19, Table II summarizes the frequencies of the dominant peaks. For $NPR > 4.5$, the peak frequency matches the dominant peak frequency in the power spectra of pressure fluctuation. This indicates that the coherent structures are a powerful acoustic source. In fact, although the mode pair (1,2) accounts for only 6%–12% of the variance, it is clearly a strong source for the pressure fluctuation. This is explained by the location of the coherent structures right downstream of the Mach disk in a region of high shear and relatively strong density gradient. Obviously, this region is a strong source of noise.

For $NPR = 4.5$, the characteristic frequency of a_1 and a_2 is about three times lower than the dominant pressure frequency. However, the measured pressure frequency matches the characteristic

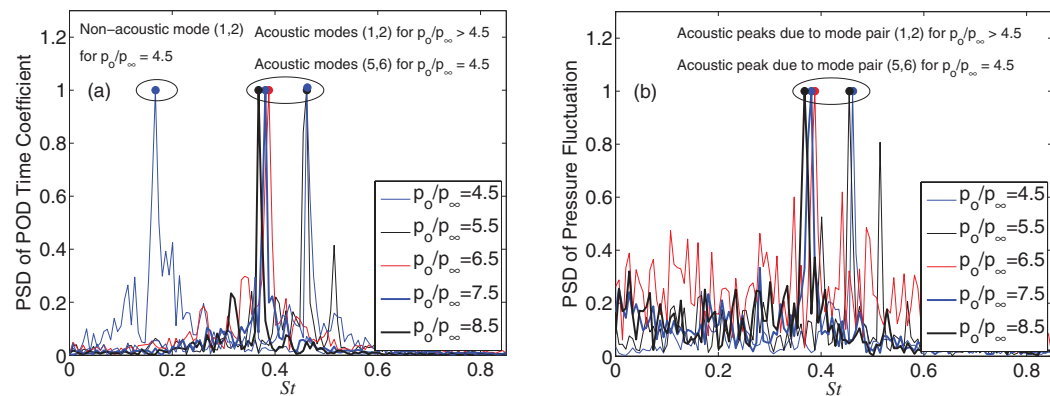


FIG. 19. (a) The spectra of POD time coefficients. (b) The spectra of pressure fluctuation sampled outside of the turbulent region at $z/D = 10$, $r/D = 3$.

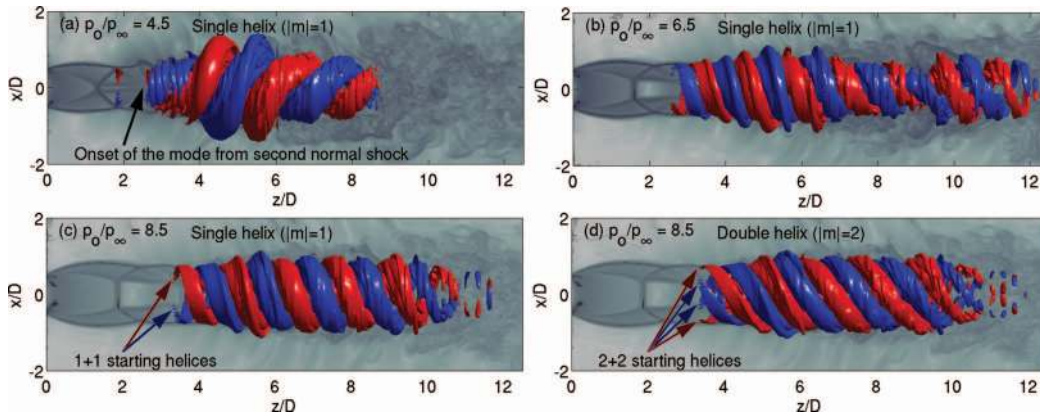


FIG. 20. The helical density modes in 3d constructed from the 2d mode pair (1,2) using the phase function. (a) $p_o/p_\infty = 4.5$, $|m| = 1$, (b) $p_o/p_\infty = 6.5$, $|m| = 1$, (c) $p_o/p_\infty = 8.5$, $|m| = 1$, and (d) $p_o/p_\infty = 8.5$, $|m| = 2$.

frequency of mode pair (5,6) indicating that this mode pair strongly influences sound emission. It should be noted that in this case, mode pair (5,6) contributes to approximately 4% of the variance but despite of their relatively low intensity, they have a clear link to the sound emission. We note that the observed peak frequency range is in line with the literature data⁴ from the viewpoint of dominant flow generated Strouhal numbers decreasing with NPR . For the present converging nozzle, also the range of the flow generated peak Strouhal numbers is close to the experimentally observed range reported by Munday *et al.* for converging-diverging nozzles.⁴

The spatial structure of the dominant POD modes corresponds to a helical mode. Combining the harmonic behavior of a rotation and the axial motion gives a phase function $P(k_z z + |m|\theta - \omega t)$ where θ is the azimuthal angle, k_z is the axial wavenumber, $|m|$ is the azimuthal wave number and ω is the pulsation angular frequency. The pulsation is related to $St \sim \omega/2\pi$ and from Fig. 16, we have $k \sim \pi/D$ for $NPR = 4.5$ and $k \sim 2\pi/D$ otherwise. The antisymmetry shown earlier for mode pair (1,2) gives an azimuthal wavenumber $|m| = 1$ and characterizes the helical mode. Gutmark *et al.*⁴⁹ reported that the dominant mode in a similar configuration satisfied $|m| = 1$, supporting the present finding. However, they did not reveal the helical nature of the mode nor characterize the spatial extent. It is noted that the phase velocity $\frac{\omega}{k} \approx 0.8U_1$ for all the cases. Since the pulsation frequency was found to be a constant, the group velocity $\frac{d\omega}{dk} \approx 0$, indicating an absolute instability. These findings are well in line with helical modes appearing in swirling flows.³⁶

At a fixed instant of time t , the phase function can be used to construct a 3d visualization out of the 2d mode in (z, r, θ) space. In particular, the angular location and time are related. The field can then be converted from cylindrical into Cartesian coordinates. Fig. 20 shows a 3d view of the helical modes as an iso-surface of the density component constructed using the mode pair (1,2). The blue and red iso-surfaces show the same iso-level but with opposite signs. The double helix shape of opposite sign is common to all cases for mode pair (1,2). For $NPR = 4.5$, the envelope of the helices expands to reach a maximum of about $3D$ at $z/D \approx 5$. The axial extent of the helix is about $8D$. For higher NPR , the envelop shows a rather constant diameter of $\approx 2D$. In these cases, the helices start after the second normal shock at the slip lines and the helices follow closely the density gradient and the annular shear-layers. The helices show a well characterized absolute instability with two leading branches being always located at the same axial location and rotating. In addition to the observed azimuthal modes $|m| = 1$, an example construction of the harmonic mode featuring $|m| = 2$ is shown for $NPR = 8.5$ in Fig. 20(d). Similar to the dominant modes $|m| = 1$, helices of opposite sign (2+2 in this case) issue at the slip lines. The four leading branches rotate but stay at the same axial location in time. The present findings give strong support to previous findings by for example Munday *et al.*⁴ who concluded that the pressure fluctuations in the region $5 \leq z/D \leq 10$ form the source for the shock-associated noise. The location of the POD modes and the provided link between the dominant frequencies evidence the significance of the helical mode in the noise production.

IV. CONCLUSIONS

The present work had four objectives. First, a LES gas jet injection model was to be developed for fuel jet studies. To our best knowledge, the present study provides the first systematic assessment on the pressure ratio dependency of highly underexpanded jet structure using LES. Second, we wanted to further assess the recommendations by Pirozzoli³¹ in developing low-dissipative numerical methods for LES of high speed flows on unstructured grids. We applied the new SSD scheme by Vuorinen *et al.*³⁴ in supersonic flows. Third, we wanted to reproduce the classical structures of high pressure jets including the Mach disk, the barrel shock, reflected shock waves and a sequence of shock cells. The dimensions of the Mach disk were in close agreement with previous literature.^{45,46} Fourth, our aim was to use POD in supersonic jets and link the dominant jet structures and frequencies with NPR and to the dominant acoustic peaks in the pressure spectra. To our knowledge POD of underexpanded jets has not been carried out previously.

The main quantitative findings of this work are summarized in Table II where the Mach disk dimensions, annular shear layer thickness, shock reflection angle and peak Strouhal numbers are reported. The new physics in the present study involves the POD modes and the investigation of transient development of the shocks. Also LES of highly underexpanded jets is a rather new topic itself and many of the results reported herein have not been investigated with such detail in previous experimental studies.

Other new findings of the work are summarized as follows: (1) A scaling law $V(t) \sim (p_o/p_\infty)^{3/4} t^{3/2}$ is proposed for the timewise volumetric expansion of the jets. This result is in agreement with the tip penetration scaling with $t^{1/2}$. (2) From global perspective, the penetration of the jet dictates the dilution of the concentration. (3) The Mach disk width $W_{disk} = W_{disk}(NPR)$ was noted to increase rapidly around $NPR \approx 5$. The consequent increase of slip line separation distinguishes highly underexpanded jets from lower pressure jets when the co-annular nature of the shear layers becomes emphasized. (4) The co-annular shear layers at higher NPR induce smaller vortex structures than seen for lower NPR as seen in POD. (5) The dominant structures indicate a helical mode. The spatial location and shown dynamics of the mode strongly complements the previously existing picture on noise production.⁴ (6) The peak frequencies of the POD coefficients explain the peak frequencies of the pressure fluctuation. The decrease of the observed peak Strouhal numbers with NPR as well as the St range of the peaks matches well the picture from the literature.⁴

As the present study showed, orthogonal decompositions can shed significant light to the physics of supersonic jets. Our future research will involve studies on mixing of cold high speed jets in hot environments which is a situation close to reality in DI NG engines. POD will certainly be used also in the upcoming studies.

ACKNOWLEDGMENTS

The study has been funded by the postdoctoral program of the Aalto University. The computational resources for this study were provided by CSC, the Finnish IT Center for Science Ltd. The study has benefited from three travel grants provided by the HPC-Europa2 project.

¹ C. D. Donaldson and R. S. Snedeker, "A study of free jet impingement. Part 1. Mean properties of free and impinging jets," *J. Fluid Mech.* **45**, 281–319 (1971).

² K. Bülent and M. V. Ötügen, "Scaling parameters of underexpanded supersonic jets," *Phys. Fluids* **14**, 4206–4215 (2002).

³ S. G. Chuech, M.-C. Lai, and G. M. Faeth, "Structure of turbulent sonic underexpanded free jets," *AIAA 26th Aerospace Sciences Meeting*, Reno, Nevada, 1988.

⁴ D. Munday, E. Gutmark, J. Liu, and K. Kailasanath, "Flow structure and acoustics of supersonic jets from conical convergent-divergent nozzles," *Phys. Fluids* **23**, 116102 (2011).

⁵ A. Dauptain, B. Cuenot, and Y. M. Gicquel, "Large-eddy simulation of a stable supersonic jet impinging on flat plate," *AIAA J.* **48**(10), 2325–2337 (2010).

⁶ T. J. S. Jothi and K. Srinivasan, "Role of initial conditions on noise from underexpanded pipe jets," *Phys. Fluids* **21**, 066103 (2009).

⁷ J. Panda and G. Seasholtz, "Measurement of shock structure and shock-vortex interaction in underexpanded jets using Rayleigh scattering," *Phys. Fluids* **11**, 3761 (1999).

⁸ K. Wohletz and G. Heiken, *Volcanology and Geothermal Energy* (University of California Press, Berkeley, 1992), Chap. 1, p. 29.

- ⁹ V. V. Golub, D. I. Baklanov, T. V. Bazhenova, M. V. Bragin, S. V. Golovastov, M. F. Ivanov, and V. V. Volodin, "Shock-induced ignition of hydrogen gas during accidental or technical opening of high-pressure tanks," *J. Loss Prev. Process Ind.* **20**(4–6), 439–446 (2007).
- ¹⁰ P. G. Hill and P. Ouellette, "Transient turbulent gaseous fuel jets for diesel engines," *J. Fluids Eng.* **121**, 93–101 (1999).
- ¹¹ P. Ouellette and P. G. Hill, "Turbulent transient gas injections," *J. Fluids Eng.* **122**, 743–753 (2000).
- ¹² T. R. White and B. E. Milton, "Shock wave calibration of underexpanded natural gas fuel jets," *Shock Waves* **18**, 353–364 (2008).
- ¹³ J. Yu, V. Vuorinen, H. Hillamo, O. Kaario, and M. Larmi, "An experimental investigation on the flow structure and mixture formation of low pressure ratio wall-impinging jets by a natural gas injector," *J. Nat. Gas Sci. Eng.* **9**, 1–10 (2012).
- ¹⁴ J. Yu, V. Vuorinen, H. Hillamo, O. Kaario, and M. Larmi, "An experimental investigation on high pressure pulsed jets for DI gas engine using planar laser-induced fluorescence (PLIF)," SAE Technical Paper Series, 2012-01-1655, 2012.
- ¹⁵ V. Vuorinen, H. Hillamo, O. Kaario, M. Nuutinen, M. Larmi, and L. Fuchs, "Large-eddy simulation of droplet Stokes number effects on mixture quality in fuel sprays," *Atomization Sprays* **20**, 435–451 (2010).
- ¹⁶ V. Vuorinen, A. Wehrfritz, J. Yu, O. Kaario, M. Larmi, and B. Boersma, "Large-eddy simulation of subsonic jets," *J. Phys.: Conf. Ser.* **318**, 032052 (2011).
- ¹⁷ E. Garnier, N. Adams, and P. Sagaut, *Large Eddy Simulation for Compressible Flows* (Springer, 2009).
- ¹⁸ J. Kim and H. Choi, "Large eddy simulation of a circular jet: effect of inflow conditions on the near field," *J. Fluid Mech.* **620**, 383–411 (2009).
- ¹⁹ M. Olsson and L. Fuchs, "Large eddy simulation of the proximal region of a spatially developing circular jet," *Phys. Fluids* **8**, 2125–2137 (1996).
- ²⁰ B. J. Boersma, G. Brethouwer, and F. T. M. Nieuwstadt, "A numerical investigation on the effect of the inflow conditions on the self-similar region of a round jet," *Phys. Fluids* **10**, 899–909 (1998).
- ²¹ C. Bogey and C. Bailly, "A family of low dispersive and low dissipative explicit schemes for flow and noise computations," *J. Comput. Phys.* **194**, 481–491 (2004).
- ²² B. J. Boersma, "A staggered compact finite difference formulation for the compressible Navier-Stokes equations," *J. Comput. Phys.* **208**, 2 (2005).
- ²³ C. Bogey, N. de Cacqueray, and C. Bailly, "A shock-capturing methodology based on adaptive spatial filtering for high-order non-linear computations," *J. Comput. Phys.* **228**, 1447–1465 (2009).
- ²⁴ N. de Cacqueray, C. Bogey, and C. Bailly, "Investigation of a high Mach number overexpanded jet using large-eddy simulation," *AIAA J.* **49**, 10 (2011).
- ²⁵ S. Kawai, S. Shankar, and K. Lele, "Assessment of localized artificial diffusivity scheme for large-eddy simulation of compressible turbulent flows," *J. Comput. Phys.* **229**, 1739–1762 (2010).
- ²⁶ S. Kawai and K. Lele, "Large-eddy simulation of jet mixing in supersonic crossflows," *AIAA J.* **48**, 2063–2083 (2010).
- ²⁷ Z. A. Rana, B. Thornber, and D. Drikakis, "Transverse jet injection into a supersonic turbulent cross-flow," *Phys. Fluids* **23**, 046103 (2011).
- ²⁸ A. Cook and W. Cabot, "Hyperviscosity for shock-turbulence interactions," *J. Comput. Phys.* **203**(2), 379–385 (2005).
- ²⁹ A. Bhagatwala and S. Lele, "A modified artificial viscosity approach for compressible turbulence simulations," *J. Comput. Phys.* **228**, 4965–4969 (2009).
- ³⁰ A. Mani, J. Larsson, and P. Moin, "Suitability of artificial bulk viscosity for large-eddy simulation of turbulent flows with shocks," *J. Comput. Phys.* **228**, 7368–7374 (2009).
- ³¹ S. Pirozzoli, "Numerical methods for high-speed flows," *Annu. Rev. Fluid Mech.* **43**, 163–194 (2011).
- ³² Z. Pouransari, G. Brethouwer, and A. V. Johansson, "Direct numerical simulation of an isothermal reacting turbulent wall-jet," *Phys. Fluids* **23**, 085104 (2011).
- ³³ L.-W. Chen, G.-L. Wang, and X.-Y. Lu, "Numerical investigation of a jet from a blunt body opposing a supersonic flow," *J. Fluid Mech.* **684**, 85–110 (2011).
- ³⁴ V. Vuorinen, P. Schlatter, L. Fuchs, M. Larmi, and B. Boersma, "A low-dissipative, scale-selective discretization scheme for the Navier-Stokes equations," *Comput. Fluids* **70**, 195–205 (2012).
- ³⁵ C. Duwig, M. Salewski, and L. Fuchs, "Large eddy simulation of a turbulent flow past two symmetric backward-facing steps: a sensitivity analysis," *AIAA J.* **46**(2), 408–419 (2008).
- ³⁶ C. Duwig and E. Gutmark, "Large scale rotating motions in a multiple jets," *Phys. Fluids* **20**, 041705 (2008).
- ³⁷ C. Duwig and L. Fuchs, "Large eddy simulation of vortex breakdown/flame interaction," *Phys. Fluids* **19**, 075103 (2007).
- ³⁸ C. Fureby and F. F. Grinstein, "Large eddy simulation of high-Reynolds-number free and wall-bounded flows," *J. Comput. Phys.* **181**, 1, 68–97 (2002).
- ³⁹ F. F. Grinstein and C. Fureby, "Recent progress on MILES for high Reynolds number flows," *J. Fluids Eng.* **124**, 848 (2002).
- ⁴⁰ L. G. Margolin, P. K. Smolarkiewicz, and A. A. Wyszogrodzki, "Implicit turbulence modeling for high Reynolds number flows," *J. Fluids Eng.* **124**, 862 (2002).
- ⁴¹ A. Chatterjee, "An introduction to the proper orthogonal decomposition," *Curr. Sci.* **78**(7), 808–817 (2000).
- ⁴² G. Berkooz, P. Holmes, and J. L. Lumley, "The proper orthogonal decomposition in the analysis of turbulent flows," *Annu. Rev. Fluid Mech.* **25**, 539–575 (1993).
- ⁴³ L. Sirovich, "Turbulence and the dynamics of coherent structures. Part 1: Coherent structures," *Quart. Appl. Math.* **XLV**(3), 561–571 (1987).

- ⁴⁴J. Borée, “Extended proper orthogonal decomposition: a tool to analyse correlated events in turbulent flows,” *Exp. Fluids* **35**, 188–192 (2003).
- ⁴⁵H. Ashkenaz and F. S. Sherman, *Rarefied Gas Dynamics*, edited by J. H. de Leeuw (Academic, New York, 1966), Vol. 1, p. 84.
- ⁴⁶B. C. R. Ewan and K. Moodie, “Structure and velocity measurements in underexpanded jets,” *Combust. Sci. Technol.* **45**, 275–288 (1986).
- ⁴⁷K. E. Meyer, J. M. Pedersen, and O. Özcan, “A turbulent jet in crossflow analyzed with proper orthogonal decomposition,” *J. Fluid Mech.* **583**, 199–227 (2007).
- ⁴⁸H. Görtler, “Dreidimensionales zur stabilitätstheorie laminarer grenzschichten,” *J. Appl. Math.* **35**, 362–363 (1955).
- ⁴⁹E. Gutmark, K. C. Schadow, and C. J. Bicker, “Mode switching in supersonic circular jets,” *Phys. Fluids A* **1**, 868 (1989).